Available online at www.sciencedirect.com
SCIENCE DIRECT®
Nuclear Instruments and Methods in Physics Research B 227 (2005) 22–31
NIM B
Beam Interactions with Materials & Atoms
www.elsevier.com/locate/nimb

Lithium fluoride (LiF) crystal for parametric X-ray (PXR) production

B. Sones *, Y. Danon, R.C. Block

Gaerttner LINAC Laboratory, Mechanical, Aerospace and Nuclear Engineering Department, Rensselaer Polytechnic Institute, Troy, NY 12180-3590, USA

Received 17 December 2003; received in revised form 18 March 2004

Abstract

Parametric X-ray (PXR) production is reported using lithium fluoride (LiF) as a target crystal interacting with 56 MeV electrons from the Rensselaer Polytechnic Institute (RPI) linear accelerator. Target crystals of Si, Ge, W, Cu, HOPG (graphite), and LiF have been studied. LiF shows the most promise for achieving an intense, quasi-monochromatic X-ray source for energies less than 40 keV. At these energies, photon absorption demands a low Z PXR target crystal for optimum yield. While HOPG graphite also meets this criterion, LiF can produce PXR with an energy linewidth narrower than achievable with graphite with 0.4° mosaic spread and at larger Bragg angles than necessary to produce equivalent PXR energies with graphite. PXR from 1.5 mm-thick LiF crystals is produced with electron beam currents up to 1.3 μA. Bragg and Laue geometries for PXR production with large LiF crystals (5 cm diameter) are compared for their Bremsstrahlung production. Reflection of PXR using a second crystal was experimentally performed.

Keywords: Parametric X-rays; LiF; Graphite; Imaging; Linac

1. Introduction

Parametric X-rays (PXR) are generated from the interaction of relativistic electrons with the periodic structure of single crystals. A broad energy distribution of "virtual photons" is associated with electrons moving through a condensed medium at relativistic speeds [1]. These photons diffract from crystallographic planes according to Bragg's Law, which relates photon energy, d-spacing between crystal planes, and the diffraction angle. For a fixed detector location, energy-tunable X-ray production is possible with simply the rotation of a target crystal about the Bragg condition. This phenomenon was first demonstrated in 1985 at the Tomsk synchrotron when Baryshevsky et al. used 900 MeV electrons interacting with a diamond (2 2 0) crystal plane to produce 6.96 keV PXR [2]. Since then, there have been several efforts to characterize the PXR photon distribution and the polarization

* Corresponding author.
E-mail address: sonesb@rpi.edu (B. Sones).

0168-583X/$ - see front matter © 2004 Elsevier B.V. All rights reserved.
doi:10.1016/j.nimb.2004.05.008

of PXR [3–7]. Other efforts have capitalized on the tunability of PXR to propose applications in material detection using near K-edge transmission measurements [8] as well as improvements to mammography configurations [9].

Experimentally, the typical targets crystals have been diamond, graphite (HOPG), silicon, germanium, and more recently tungsten because of its higher PXR production efficiency [10]. However, the PXR production mechanism in a crystal competes with the absorption of PXR along the escape path in the crystal. In general, PXR production efficiency is proportional to Z^2, but the PXR absorption length decreases proportional to Z^{-4}, where Z is the crystal atomic number Z [10]. For higher Z materials, the absorption losses increase more rapidly than the PXR production [11]. This makes low Z target crystals preferable to high Z crystals; experimental results comparing low and high Z target crystal PXR yields were done by Sones et al. at RPI [12]. Other considerations for the PXR optimization process include the PXR energy, and crystal atomic number, thickness, planes, and geometry. The first observation of PXR from LiF is discussed in an unpublished results found in a Master's thesis supervised by X. Maruyama in 1995 [18]. The aim of this paper is to point out the advantages of using LiF for the production of tunable X-rays to be used for medical imaging applications.

2. Theory

The production of PXR can be visualized from Fig. 1. In this drawing, a relativistic electron moves from left to right to interact with crystallographic planes with some distance d between planes. The reciprocal lattice vector for these planes is shown as $\vec{\tau}$. A virtual photon field is associated with a relativistic electron traversing a crystal. The primary momentum direction of the photon field is in the direction of the electron's velocity. Bragg's Law $\left(\vec{\tau} = \vec{k}_{\mathrm{f}} - \vec{k}_{\mathrm{i}}\right)$ defines the diffraction of the virtual photons to produce real photons emitted from the crystal. After a Lorentz transformation, the relativistic electron's electric field is distorted to the well-known disk shape [1]. This characterizes the cone-like shape of the emitted PXR.

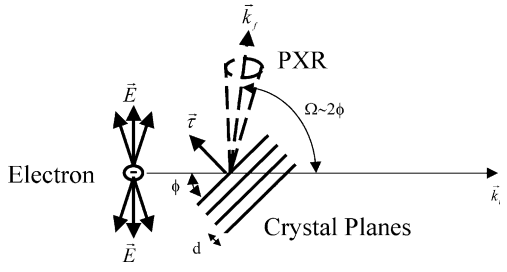

Fig. 1. Drawing of electron interaction with crystallographic planes to produce parametric X-rays.

Also shown in Fig. 1 are the electron incident angle (ϕ) with respect to the crystal planes and the PXR emission angle (Ω) with respect to the electron velocity. Bragg's law is satisfied for the condition $\Omega = 2\phi$ around which produces the maximum PXR intensity. Nonetheless, PXR is still produced with some mismatch between Ω and 2ϕ, and this feature allows for PXR energy tunability in experiments with changes in either Ω or ϕ or both angles. The expression for calculating the PXR energy is shown below [7]:

$$E_{\mathrm{PXR}} = \hbar\omega_{\mathrm{PXR}} = \hbar c \frac{\tau \sin\phi}{1 - \cos\Omega}. \tag{1}$$

The photon distribution of PXR at positions near the Bragg condition is typically expressed in the solid angle described by angular displacement from the Bragg condition in the diffraction plane (θ_x) and perpendicular to the diffraction plane (θ_y). While it is common to use units convenient for quantum electrodynamics ($h = c = 1$), the MKS expression for the photon distribution of PXR [photons per electron per steradian] is shown below [13]:

$$\frac{\mathrm{d}^2 N}{\mathrm{d}\theta_x \mathrm{d}\theta_y} = \frac{\alpha}{4\pi}\frac{\omega_{\mathrm{B}}}{c} f_{\mathrm{geo}} \chi^2 \mathrm{e}^{-2W} \times \frac{\theta_x^2 \cos^2 2\theta_{\mathrm{B}} + \theta_y^2}{\sin^2\theta_{\mathrm{B}}\left(\theta_x^2 + \theta_y^2 + \theta_{\mathrm{ph}}^2\right)^2}, \tag{2}$$

with α the fine structure constant, ω_{B} the PXR angular frequency, θ_{B} the Bragg angle and e^{-2W} the Debye–Waller factor which accounts for thermal

lattice vibration. For electron energies less than 100 MeV, the only term in Eq. (2) relating to the electron energy is θ_{ph}, the characteristic angle which defines the spread of the cone of PXR photons where $\theta_{ph} \sim \gamma^{-1}$ (γ is the Lorentz factor). χ is the Fourier expansion of the electric susceptibility, which can be viewed as the crystal's diffraction efficiency. And f_{geo} is a geometric effect that accounts for the PXR path length through the crystal and the X-ray absorption along that path. f_{geo} is proportional to the PXR photon attenuation length, L_a. Both f_{geo} and χ depend on the PXR photon energy.

For a given PXR energy, f_{geo} and χ generally compete when one considers changes in Z of the target crystals. Generally, higher Z materials are more efficient in producing PXR but have shorter attenuation lengths compared with lower Z materials. In order to produce the largest PXR photon flux, the optimized selection of a PXR target crystal must consider the required energy and the crystal Z, thickness, lattice parameters, Debye temperature, and plane orientation with respects to the crystal surface. For example, Table 1 lists some of these parameters for the production of 15 keV PXR using a variety of target crystals.

In Table 1, the crystals are arranged in order of increasing Z. For the 15 keV PXR, the attenuation lengths L_a generally decrease with increasing Z, allowing less PXR to escape from similarly sized crystals. Likewise, the susceptibilities are observed to increase with increasing Z, allowing more PXR production from similarly sized crystals. Germanium is the only anomaly to this trend as its production efficiency is less than expected from the Z^2 proportionality trend, likely because its larger unit cell reduces its charge density. The Debye temperature also decreases with increasing Z. For high electron currents or thick crystals, heat deposited in the higher Z crystals will degrade the PXR yield more than in the low Z materials because of the increased crystal lattice vibration. Finally, the Bragg angle (θ_B) for the 15 keV PXR has no relationship to the crystal Z and is solely determined by the d-spacing of the diffraction plane. The smaller d-spacing produces larger Bragg angles, which become important in practical PXR experiments using a linear accelerator. Larger Bragg angles move the detector location farther off of the Linac electron beam direction and reduce the capture of unwanted, forward-directed Bremsstrahlung produced from the 254 μm (10 mil) Be Linac output window and the target crystal itself.

At the RPI Linac, the PXR experiments restricted the angle of the detector relative to the electron beam axis to at least 9° to minimize detection of high energy Bremsstrahlung and to avoid scattered electrons from hitting the detector. Fig. 2 has been calculated to help select target crystals for optimized PXR production at various PXR energies. This graph shows the PXR photon yield [photons/e/mm^2] for various crystal planes by integrating Eq. (2) about a 1 mm^2 detector situated

Table 1
Target crystal parameters for production of 15 keV PXR

Crystal	Bravais lattice/reflection	Z	d	ω_p, plasma frequency	L_a	χ	θ_B	Debye temperature
			[10^{-10} m]	eV	[μm]	[10^{-6}]		K
Be	Hex(0 0 0 2)	4	1.79	26	20759.0	1.300	13.34	1000
Graphite	Hex(0 0 0 2)	6	3.35	31	9144.3	3.101	7.09	1860
Diamond	FCC(1 1 1)	6	2.05	38	5849.5	2.368	11.60	1860
LiF	FCC(2 0 0)	*8.3*	2.01	32	1568.8	2.768	11.84	730
LiF	FCC(2 2 0)	*8.3*	1.42	32	1568.8	1.978	16.87	730
Si	FCC(1 1 1)	14	3.14	31	443.7	2.271	7.57	625
Si	FCC(2 2 0)	14	1.92	31	443.7	2.271	12.43	625
Cu	FCC(1 1 1)	29	2.08	51	15.0	11.368	11.44	315
Ge	FCC(1 1 1)	32	3.27	44	20.5	5.183	7.27	360
W	BCC(1 1 0)	74	2.24	84	3.8	23.240	13.07	310
W	BCC(2 2 2)	74	0.91	84	3.8	18.940	26.88	310

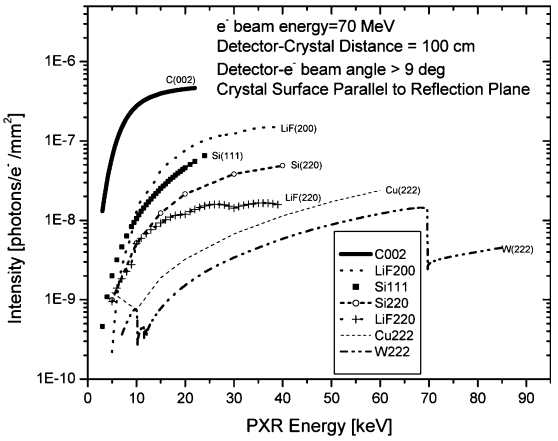

Fig. 2. Theoretical PXR photon yield for graphite, LiF, Si, Cu and W at various PXR energies.

in the diffraction plane, at the characteristic angle, and located 1 m away from the crystal at various Bragg angles. For these parameters, the integration limits are ±0.5 mrad around θ_x and θ_y. The crystal is rotated while the detector location is moved so that the Bragg condition ($\Omega = 2\phi$) is preserved, and the diffraction plane is assumed to be parallel with the crystal surface for simplicity. Because of commercial availability, the crystals are all 1 mm thick, except for the Si, which are inexpensively obtained as 0.5 mm-thick wafers. Some calculations such as graphite (0 0 2) are terminated at PXR energies for which $\Omega < 9°$.

Fig. 2 demonstrates two important features in selecting target crystals for PXR production. First, because of the 9° angle constraint, the larger d-spacing of crystals tends to limit their use for higher energy PXR production. For example, production of 50 keV PXR can only be achieved under the 9° constraint using Cu or W, but not with the remaining crystals. Second, for lower energy PXR, the photon yields from the lower Z materials can be 1–2 orders of magnitude greater than for the higher Z materials. For medical imaging of soft tissue the mean X-ray energy is typically about 20 keV [14]. In this energy region, graphite and LiF produce the largest photon yield, although graphite is marginally useful for the production of PXR under the detector angle constraint. A higher order reflection can produce the desired PXR energy, but the yield from the next higher order reflection can be as much as two orders of magnitude less than the fundamental, first order reflection.

3. Experimental setup

All PXR experiments at RPI are done in air after the electron beam has exited a 254 μm (10 mil) beryllium linear accelerator output window. An earlier water-cooled aluminum window with 1.6 mm aluminum and 1.6 mm water thickness was replaced because of electron scattering and Bremsstrahlung production. Monte-Carlo simulations as well as analytical calculations [3] suggest that a 60 MeV pencil beam of electrons will scatter from the new Be window with a Gaussian distribution with standard deviation of only 3 mrad. The predicted Bremsstrahlung from this window may be diffracted from the target crystal, but this unlikely event can be ruled out by inspection of the measured spectra. The energy of PXR and diffracted Bremsstrahlung radiation (DBR) are the same at the Bragg angle. However, the relation

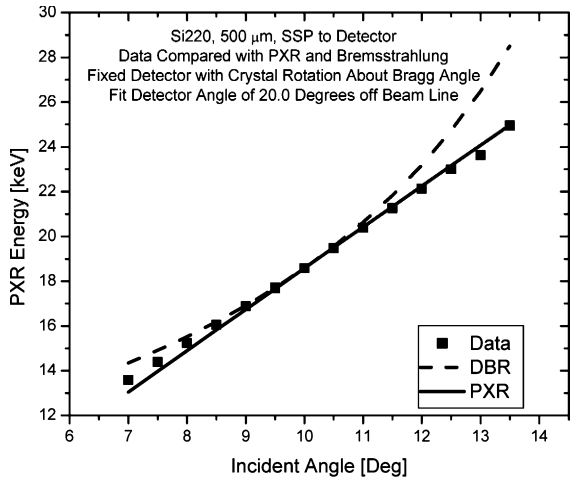

Fig. 3. Measured spectrum data compared to calculated PXR and diffracted Bremsstrahlung radiation (DBR) with target crystal rotation about a 10° Bragg angle. Target crystal is 500 μm thick Si(2 2 0).

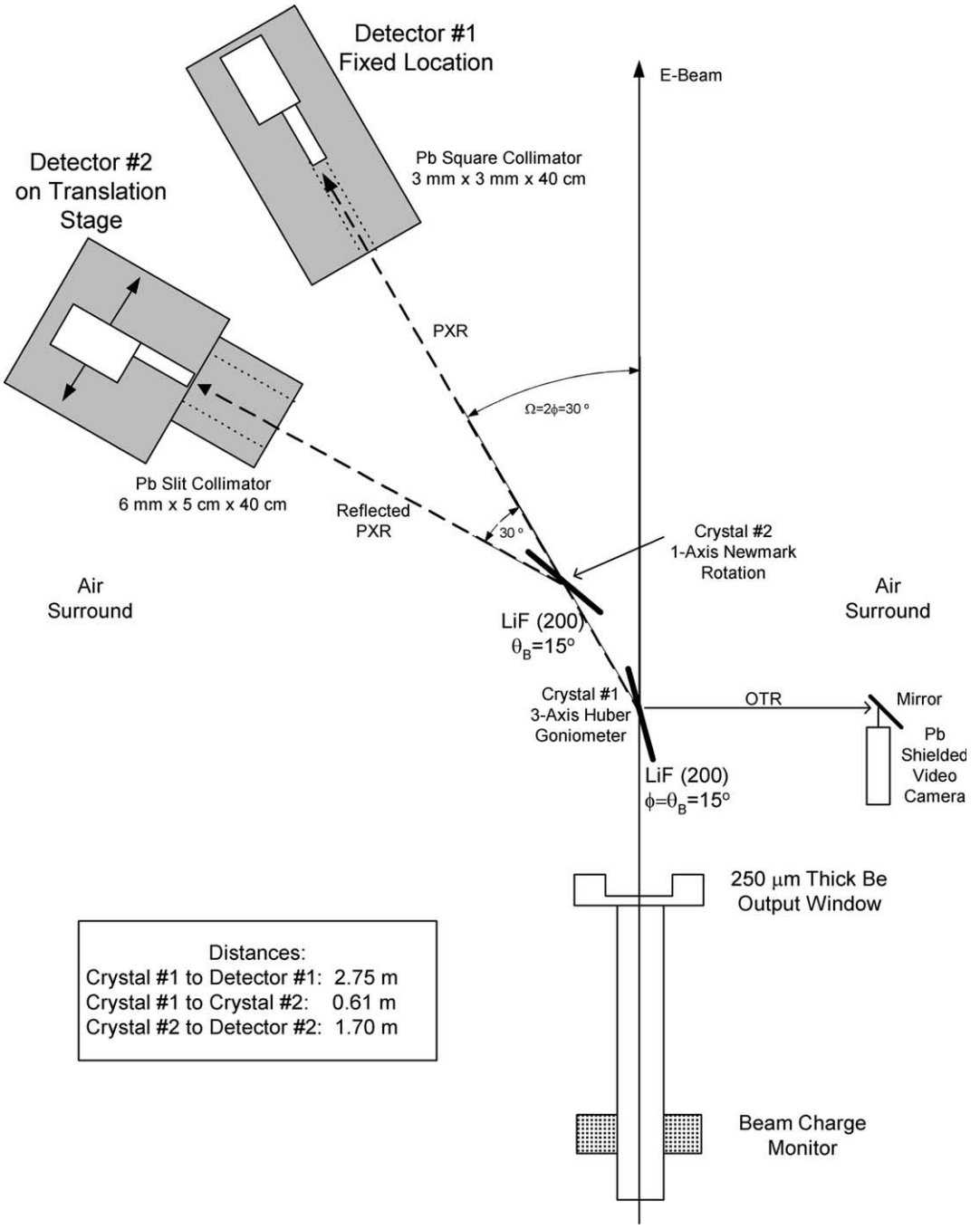

Fig. 4. Typical experimental set-up (Detector #1 and Crystal #1) shown with components of a PXR reflection experiment (Detector #2 and Crystal #2).

between the diffraction angle and the diffracted photon energy is different than the PXR energy relationship [15]. The energy of DBR is calculated with Eq. (3), the target crystal changes $\vec{\tau} \cdot \vec{\Omega}$.

$$E_{\mathrm{DBR}} = \hbar c \frac{|\vec{\tau}|^2}{2\sqrt{\varepsilon_0}\vec{\tau}\cdot\vec{\Omega}}. \quad (3)$$

Comparison of data with Eqs. (1) and (3) is routinely performed to assess the contribution of DBR to the measured spectrum. In Fig. 3, experiments with 500 μm thick Si(2 2 0) with the detector angle fixed at $\Omega = 20°$, show conclusive energy agreement with PXR for incident angles greater than the Bragg angle ($\theta_B = 10°$) where the differences between PXR and DBR are most accentuated. Thus, we can conclude that with the 254 μm Be Linac window the measured PXR spectra are not contaminated by diffracted Bremsstrahlung.

Electrons from the RPI Linac are incident on a target crystal rotated in a 3-axis goniometer to produce PXR at a well shielded, fixed detector location. The detector is a 500 μm Si Amptek XR-100CR detector with 25 mm^2 area and resolution of 350 eV at 17 keV. The detector position is based on the determined angle Ω (see Eq. (1)) for the required PXR energy. Laser alignment is used to position the detector, crystal, and detector collimation with respects to the Linac output window and electron beam direction. The detector is calibrated using fluorescence from Zn (8.64 keV), Zr (15.77 keV) and Sn (25.27 keV). The detector is heavily shielded in lead, and the output cable is encased in a copper pipe to shield from the effects of RF energy in the target room. The Linac electron beam current is determined from the Linac pulse rate and the electric charge per pulse measured by a Bergoz beam charge monitor (BCM) concentrically mounted on the electron drift tube. The electron position and spot size/shape are monitored directly on the PXR target crystal using backward optical transition radiation (OTR) viewed by a distant video camera. Electron currents were in the range from 10 nA to 1.3 μA, and the electron spot size viewed at the target crystal is approximately 1 cm radius. Electron energy is measured upstream periodically by magnetically bending the electron beam to a fixed Faraday cup. In these experiments, the typical electron energy is 56 MeV. Fig. 4 shows the experimental set-up for some data presented in this paper. Typical PXR spectra are taken with Detector #1 and the target crystal held at the goniometer. Also shown in Fig. 4 are components of a PXR reflection experiment in which a second reflecting crystal is held at the rotation stage and a second detector mounted on a translation stage measures the reflected PXR.

4. Results

PXR from LiF was first produced with a relatively small, 1 mm thick, 1 cm × 1 cm LiF crystal with surface [1 0 0] at a detection angle of 60°. This corresponds to a Bragg angle of 30° and for LiF(2 0 0) and a first order energy of 6.15 keV. Fig. 5 shows a representative spectrum of PXR from the small crystal using a Laue geometry [2 0 0] (planes perpendicular to the crystal surface). Count rates (cps) shown throughout this paper are calculated by dividing the net counts under the peak by the live time (real time – MCA deadtime). The first order PXR is observed at 6.23 keV, corresponding to a Bragg angle of 29.6°, well within the tolerance of the laser alignment techniques ±0.5°. Since the PXR travel approximately 3 m in air to the detector, the 6.23 keV first order reflection is predictably attenuated by 3 orders of magnitude. Therefore, the second order reflection LiF(4 0 0) appears the most intense.

In order to measure the same spectrum in the Bragg geometry (planes parallel to the crystal

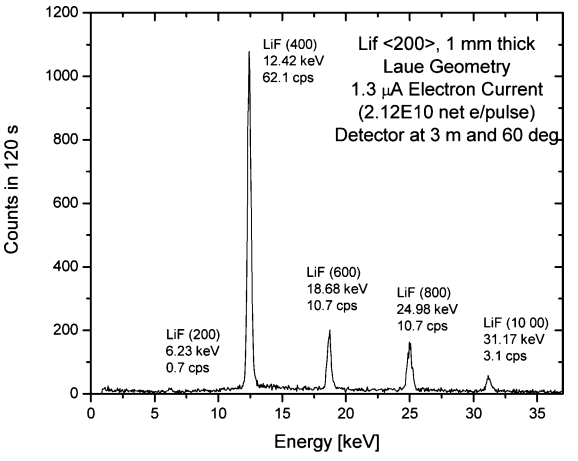

Fig. 5. Small LiF crystal PXR in the Laue geometry with Bragg angle (ϕ) of 30°.

surface) the crystal is rotated by 90°. In the Laue geometry, the count rate in the LiF(4 0 0) reflection (62 cps) was nearly twice that measured in the Bragg geometry (37 cps) despite the expected smaller yield as a result of a slightly longer PXR path length in the crystal. The crystal is smaller than the electron beam and the rotation of crystal affects its electron beam capture area. With these small crystals, the difference in the count rates between the Laue and Bragg geometries is attributable to the difference in number of electron interactions.

PXR was also produced with highly oriented pyrolytic graphite (HOPG) with the same dimensions as the small LiF crystal discussed above. The two spectra compared in Fig. 6 are intended to demonstrate the effects of mosaic spread on the PXR energy linewidth. The resolution of the Si detector is 350 eV at 17.5 keV (~2%), which typically dominates the observed PXR energy linewidth from all tested crystals except for graphite. We used HOPG with a mosaic spread of 0.4° measured with the K_α fluorescence line of Cu. The measured energy linewidth of the PXR from HOPG (0 0 2) is 6.25% compared to 2.63% for comparable energies with LiF(4 0 0). While the PXR yield from graphite is greater, the energy linewidth (FWHM) of the PXR is greater than PXR from LiF.

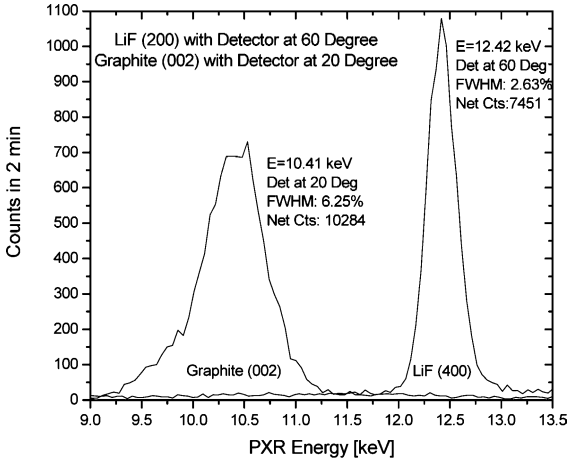

Fig. 6. Comparison of graphite and LiF PXR energy linewidths at energies near 10 keV.

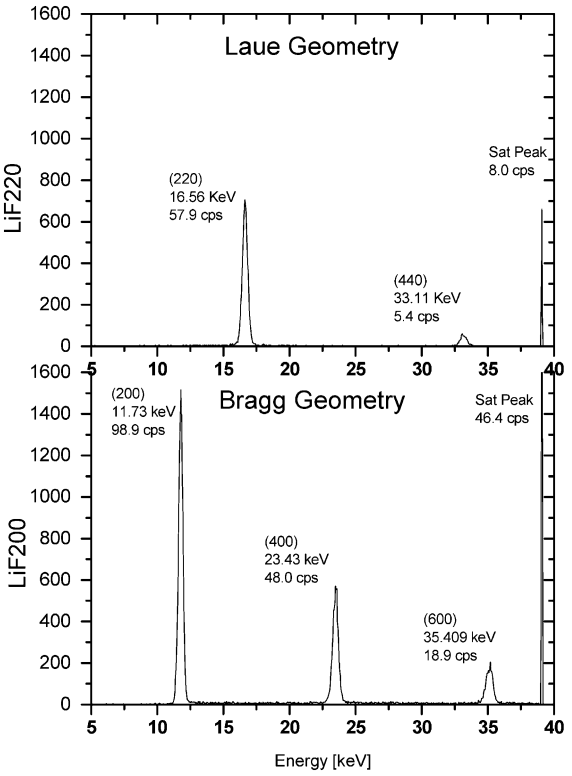

Fig. 7. Comparison of LiF(2 2 0) in Laue geometry and LiF(2 0 0) in Bragg geometry using 1.5 mm thick crystal with 12.8 nA electron beam current.

Experiments were also performed with larger LiF crystals and are shown in Fig. 7. Calculations using Eq. (2) suggested that a thicker LiF crystal could produce more PXR, make full use of the relatively large electron beam spot, and provide the structural stability to have a ⟨1 1 0⟩ flat for easy crystal orientation. MTI Corporation supplied LiF crystals with 1.5 and 4.0 mm thickness, 5.0 cm diameter with surface [1 0 0], and a ⟨1 1 0⟩ flat. The flat allows for easy alignment with the (2 2 0) plane as well as the (2 0 0) plane using the surface Bragg reflection. As expected, the larger LiF crystal produced more PXR than the smaller LiF crystal. However, in the Bragg geometry the larger crystal had a larger electron path length in which was generated unwanted Bremsstrahlung. Presence of high-energy Bremsstrahlung and fluorescence from Pb is observed in the background shown in the last channel of the multi-channel analyzer (MCA)

(later referred as the "saturation peak") in which all measured photons above 39 keV are counted. Fig. 7 shows two large LiF crystal PXR spectra for Bragg angle of 15°: one for a Laue geometry LiF(2 2 0) for which a pencil-beam electron would traverse approximately 1.5 mm of LiF, another for a Bragg geometry LiF(2 0 0) and an electron traveled distance of approximately 5.8 mm in LiF. To first order, the ratio of electron path lengths (4:1) closely resembles the ratio of photons counted in the saturation peak (6:1).

Minimizing the counts in this saturation peak is necessary in order to reduce the effects of detector dead time and to achieve spectral purity for X-ray imaging. Detector dead time is increased by counts in this saturation peak, and a model for dead time correction has been developed for PXR experiments and other spectroscopy experiments [16]. Note that all count rates (cps) for spectra shown in this paper are uncorrected measured data. Comparing these LiF Bragg and Laue geometries, the LiF(2 0 0) produces more PXR than the LiF(2 2 0) consistent with theoretical predictions in Fig. 2. However, the lower photon yield from LiF(2 2 0) may be a favorable geometry because of its reduced Bremsstrahlung production. Monte-Carlo simulations with MCNP-4C2 [17] provide the ability to verify this result. Calculations of the Bremsstrahlung photon flux at a detector position produced from a pencil-beam of 56 MeV electrons striking the center of the LiF crystal are performed under the experimental conditions for the data shown in Fig. 7. Fig. 8 shows the MCNP-4C2 results for the Bremsstrahlung produced from the LiF crystal in the Bragg and Laue geometries, and the ratio of total Bremsstrahlung produced (4:1) is consistent with the results in Fig. 7.

With LiF(2 2 0) in the Laue geometry, the face of the crystal is exposed to the Bremsstrahlung from the Be window. Again, measurements with rotation of the crystal about the Bragg angle can assess the impact of diffracted Bremsstrahlung radiation in the detected spectra. Fig. 9 shows the comparison of data with calculated PXR and DBR energies for LiF(2 2 0) orientations to the electron beam with the detector fixed at 30° to the electron beam. As with the thin Si crystal, diffracted Bremsstrahlung produced by the Be window does not contribute to the measured spectra during the RPI PXR experiments. Even though this confirms the PXR production mechanism for the measured LiF spectra, diffracted Bremsstrahlung from the window or other radiators may be useful in future imaging applications.

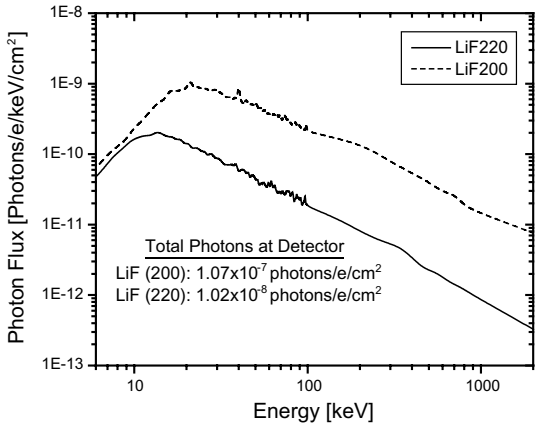

Fig. 8. MCNP-4C2 calculation of Bremsstrahlung at the detector during PXR experiments involving the interaction of 56 MeV electrons with 1.5 mm thick, 5 cm diameter LiF crystals in the Laue (2 2 0) and Bragg (2 0 0) geometries with $\phi = 15°$.

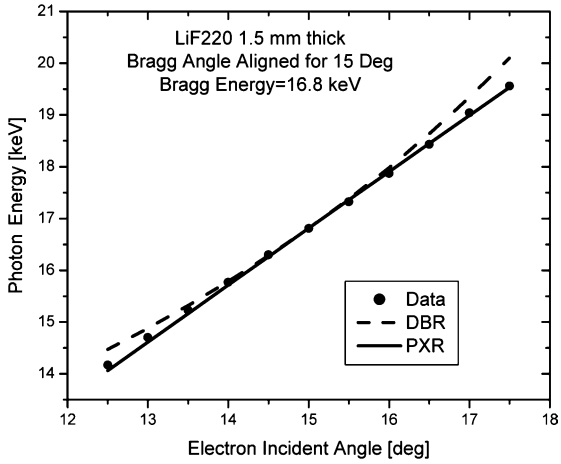

Fig. 9. Measured spectrum data compared to calculated PXR and diffracted Bremsstrahlung radiation (DBR) with target crystal rotation about a 15° Bragg angle. Target crystal is 1.5 mm thick LiF(2 2 0).

The last part of this investigation with LiF was to assess whether the Bremsstrahlung photons and any other unwanted photons could be removed

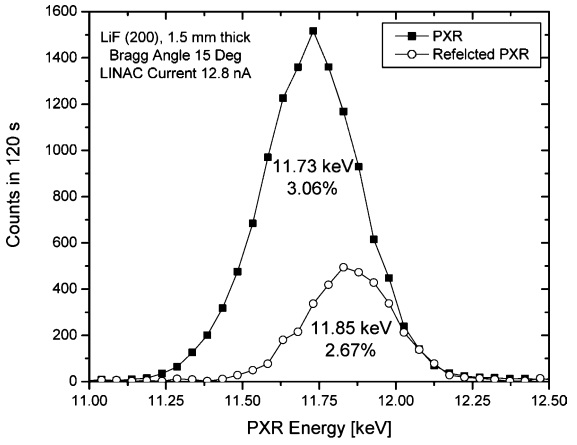

Fig. 10. Spectra of LiF(2 0 0) PXR measured at Detector #1 and reflected PXR measured at Detector #2.

from the PXR spectrum by reflection using an additional crystal. This experiment included a LiF target crystal for PXR production and a second LiF analyzer for PXR reflection. The set-up is shown in Fig. 4 in which Crystal #2 and Detector #2 are employed. The LiF(2 0 0) plane was used for both PXR production and reflection. Lasers were used to insure proper alignment. Crystal #2 could be rotated about a vertical axis but not translated from its aligned position. Detector #2 is shielded behind a 6 mm horizontal slit, 5 cm long and 40 cm deep; Detector #2 is centered on the horizontal slit and can translate the 5 cm length of the slit while facing Crystal #2. Fig. 10 shows both the PXR measured at Detector #1 and the reflected PXR measured at Detector #2. The process of these measurements starts with the optimized PXR production through rotations of Crystal #1 to establish the Crystal #1 Bragg angle for PXR measured by Detector #1. Then with Crystal #1 fixed, rotations of Crystal #2 and translations of Detector #2 are necessary to optimize the measurement of the reflected PXR. In practice, an intermediate step of rotating Crystal #1 was necessary to first find evidence of the reflected PXR at Detector #2 before optimizing the reflected signal. Spectra shown in Fig. 10 are with Crystal #1 returned to the Bragg angle and with the best efforts to optimize the reflected PXR. While this experiment succeeded in measuring reflected PXR, it also failed in other respects. First, despite the laser alignment, rotation of Crystal #2, and translation of Detector #2, the precise reflection of the incident PXR on Crystal #2 could not match the primary PXR energy nor efficiently reflect most of the PXR. Notice the mismatch of centroid energies and the difference in the number of measured photons between the PXR and reflected PXR peaks. Second, the reduction of reflected PXR came with no dramatic reduction of counts in the saturation peak of the MCA; the reflection did not clean the PXR spectrum of the unwanted Bremsstrahlung noise. This is likely due to the larger slit collimation necessary to translate Detector #2 for optimal alignment. Finally, since the same crystal and plane were used for PXR production and reflection, the unwanted higher order PXR reflections were reflected just as well as the fundamental reflection PXR. This problem can be simply resolved by reflecting with either a different plane from LiF or to use an entirely different crystal so that the primary PXR is reflected without satisfying Bragg conditions for the higher order PXR energies.

5. Conclusions

Parametric X-rays were produced using lithium fluoride as a target crystal. For PXR energies less than 40 keV, target crystals with low Z are favorable because their attenuation lengths allow for higher PXR yield and inefficient production of unwanted Bremsstrahlung. Graphite and LiF both appear most favorable for PXR use in medical and biological applications. While graphite produces more photons, there are some advantages for using LiF with linear accelerators because its d-spacing allows for PXR production at larger angles relative to the electron beam direction and the LiF PXR energy linewidth is not as severely broadened as that from graphite.

When larger diameter LiF crystals were used, there were distinct differences between the Bragg and Laue geometries because the longer effective electron path in the Bragg geometry produces more unwanted Bremsstrahlung. The efforts to clean the PXR spectrum through reflection from a second crystal may prove to be worthwhile.

However, this experimental complexity failed to address the largest PXR production problem at RPI, which continues to be the high-energy photons that are counted in the saturation peak. The solution may rest with the electron source rather than the target crystal. Some preliminary efforts in reducing these photons are being directed towards improved shielding, electron beam monitoring, and electron magnetic optics in the RPI Linac.

To conclude, these experimental studies demonstrated efficient production of PXR from thick LiF crystals (1.5 mm) irradiated with high electron beam currents (>1 μA). Both of these experimental features were steps into uncharted PXR territory, which seem necessary for practical use of PXR in a medical or biological application. There remain further investigations into the durability of LiF at higher electron beam currents and to examine the effects of electron multiple scattering in thick crystals.

References

[1] M.L. Ter-Mikaelian, High Energy Electromagnetic Processes in Condensed Media, Wiley-Interscience, New York, 1972.

[2] V.G. Baryshevshy, V.A. Danilov, O.L. Ermakovich, I.D. Feranchuk, A.V. Ivashin, V.I. Kozus, S.G. Vinogradov, Angular distribution of parametric X-rays, Phys. Lett. A 110 (1985) 477.

[3] K.H. Brenzinger, B. Limburg, H. Backe, S. Dambach, S. Euteneuer, F. Hagenbuck, C. Herberg, K.H. Kaiser, O. Kettig, G. Kube, W. Lauth, H. Schope, Th. Walcher, How narrow is the linewidth of parametric X-ray radiation? Phys. Rev. Lett. 79 (1997) 2462.

[4] A.V. Shchagin, V.I. Pritupa, N.A. Khizhnyak, A fine structure of parametric X-ray radiation from relativistic electrons in a crystal, Phys. Lett. A 148 (1990) 485.

[5] R.B. Fiorito, D.W. Rule, M.A. Piestrup, Qiang Li, A.H. Ho, X.K. Maruyama, Parametric X-ray generation from moderate energy electron beams, Nucl. Instr. and Meth. B 79 (1993) 758.

[6] S. Asano, I. Endo, M. Harada, S. Ishii, T. Kobayashi, T. Nagata, M. Muto, K. Yashida, H. Nitta, How intense is parametric X radiation? Phys. Rev. Lett. 70 (1993) 3247.

[7] T. Akimoto, M. Tamura, J. Ikeda, Y. Aoki, F. Fujita, K. Sato, A. Honma, T. Sawamura, M. Narita, K. Imai, Generation and use of parametric X-rays with an electron linear accelerator, Nucl. Instr. and Meth. A 459 (2001) 78.

[8] F. Hagenbuck, H. Backe, N. Clawiter, H. Euteneuer, F. Gorgen, P. Holl, K. Johann, K.H. Kaier, J. Kemmer, Th. Kerschner, O. Kettig, H. Kettig, H. Koch, G. Kube, W. Lauth, H. Mattay, M. Schutrumpf, R. Stotter, L. Struder, Th. Walcher, A. Wilms, C.V. Zanthier, M. Zemter, Novel digital K-edge imaging system with transition radiation from an 855-MeV electron beam, IEEE Trans. Nucl. Sci. 48 (3) (2001).

[9] M.A. Piestrup, X. Wu, V.V. Kaplan, S.R. Uglov, J.T. Cremer, D.W. Rule, R.B. Fiorito, A design of mammography units using a quasi-monochromatic X-ray source, Rev. Scientific Inst. 72 (2001) 2159.

[10] Y. Adischev, S. Arishev, A. Vnukov, A. Yukolov, A. Polyitsyn, S. Kuznetsov, V. Zabaev, B. Kalinin, V. Kaplin, S. Uglov, A. Kubankin, N. Nasonov, Angular distribution of X-ray radiation by 500 MeV electrons in an tungsten crystal, Nucl. Instr. and Meth. B 201 (2003) 114.

[11] Y. Danon, B. Sones, R. Block, Novel X-ray source at the RPI LINAC, in: Proceedings, ANS Annual Meeting, Hollywood, Florida, June 2002.

[12] B. Sones, Y. Danon, R. Block, Advances in Parametric X-ray Production at the RPI linear accelerator, in: Proceedings, ANS Annual Meeting, San Diego, California, June 2003.

[13] J. Freudenberger, H. Genz, V. Morokhovshyi, A. Richter, J. Sellschop, Parametric X-rays observed under Bragg condition: Boost of intensity by a factor of two, Phys. Rev. Lett. 84 (2000).

[14] A.B. Wolbarst, Physics of Radiology, Medical Physics Publishing, Madison, Wisconsin, 2000.

[15] A.V. Shchagin, V.I. Pristupa, N.A. Khizhnyak, Absolute differential yield of parametric X-rays radiation, in: Proceedings of the International Symposium of Radiation from Relativistic Electrons in Periodic Structures, Tomsk, Russia, 6–10 September 1993.

[16] Y. Danon, B. Sones, R.C. Block, Dead time and pileup in pulsed parametric X-rays spectroscopy, Nucl. Instr. and Meth. A 524 (2004) 287.

[17] Monte Carlo N-Particle Transport Code (MCNP4C2), Los Alamos National Laboratory, Los Alamos, New Mexico, June 2001.

[18] J.R. Thien, High order parametric X-radiation from silicon and lithium fluoride crystal monochromators, MS Thesis, Naval Postgraduate School, December 1995, Monterey, California.